Systematic Investigation of Iridium-Based Bimetallic Thin Film Catalysts for the Oxygen Evolution Reaction in Acidic Media

Strickler, Alaina L.; Flores, Raul A.; King, Laurie A.; Nørskov, Jens K.; Bajdich, Michal; Jaramillo, Thomas F.

Published in:
ACS Applied Materials and Interfaces

Link to article, DOI:
10.1021/acsami.9b13697

Publication date:
2019

Document Version
Peer reviewed version

Systematic Investigation of Iridium-Based Bimetallic Thin Film Catalysts for the Oxygen Evolution Reaction in Acidic Media

Alaina L. Strickler,[1] Raul A. Flores,[1] Laurie A. King,[1] Jens K. Nørskov[3,1,2],

Michal Bajdich,[2*] and Thomas F. Jaramillo[1,2*]

[1]Department of Chemical Engineering, Stanford University, Stanford, California 94305, United States

[2]SUNCAT Center for Interface Science and Catalysis, SLAC National Accelerator Laboratory, Menlo Park, California 94025, United States

[3]Department of Physics, Technical University of Denmark, 2800 Kongens Lyngby, Denmark

*Corresponding authors: jaramillo@stanford.edu and theory: bajdich@slac.stanford.edu

Keywords: Oxygen evolution reaction, Acidic media, Cr-doping, Density functional theory, volcano plot, theoretical overpotential, electrochemical characterization.

ABSTRACT

Multi-metallic Ir-based systems offer significant opportunities for enhanced oxygen evolution electrocatalysis by modifying electronic and geometric properties of the active catalyst. Herein, a systematic investigation of bimetallic Ir-based thin films was performed to identify activity and stability trends across material systems for the oxygen evolution reaction (OER) in acidic media. Electron beam evaporation was used to co-deposit metallic films of Ir, $IrSn_2$, IrCr, IrTi, and IrNi. The electrocatalytic activity of the electrochemically oxidized alloys was found to increase in the order of IrTi < $IrSn_2$ < Ir ~ IrNi < IrCr, with the IrCr system demonstrating two times the catalytic activity of Ir at 1.65 V vs. RHE. Density functional theory calculations suggest that this enhancement is due to Cr active sites that have improved oxygen binding energetics compared to pure Ir-oxide. This work identifies Ir-Cr as a promising new catalyst system that facilitates reduced precious metal loadings for acid-based OER catalysis.

TOC Graphic

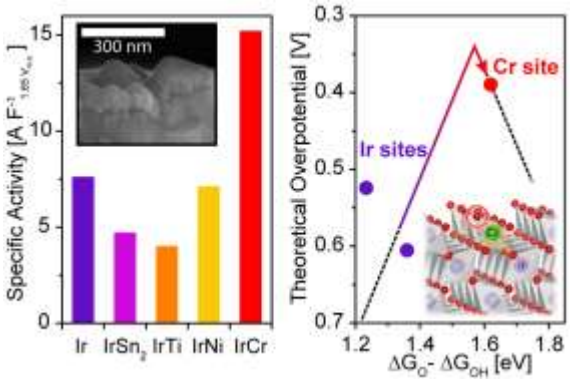

INTRODUCTION

Water electrolysis is a promising emerging technology for renewable energy storage and sustainable hydrogen production.[1–3] Hydrogen is an essential chemical commodity produced at a rate of 65 million tons annually with a demand that is forecast to increase with the continued growth of the agriculture industry and demand for emissions-free fuels.[4] While currently predominately produced from fossil-fuels with substantial CO_2 emissions,[5] hydrogen can also be produced with minimal emissions (depending on the electricity source) through electrochemical water electrolysis. Importantly, water

electrolyzers can be paired with variable sources of renewable energy as a means of energy storage to enable further penetration of renewable technologies (i.e. solar and wind) into the energy sector.[6]

For electrolytic hydrogen to become commercially competitive, however, anode catalysts must be improved to increase the efficiency of the kinetically-limited oxygen evolution reaction (OER) and reduce electricity and catalyst costs.[1–3] While alkaline water electrolyzer systems allow for a variety of earth-abundant high-performance catalysts,[2,7,8] proton exchange membrane (PEM) electrolyzers currently provide higher current densities, improved efficiencies, and greater product purity.[9] However, the highly acidic and corrosive environment of a PEM electrolyzer places severe limitations on applicable catalyst materials.[2,7] Rare, precious-metal Ir-based materials remain the only industrially relevant OER catalysts in acidic media due to their relatively high activity and stability.[2] Still, Ir catalysts lack the performance to obtain competitive hydrogen costs compared to fossil-derived hydrogen, requiring large applied voltages and high catalyst loadings.[10,11]

Although Ir-oxides exhibit the best balance between activity and stability of known materials to date, Ir-oxide has suboptimal oxygen intermediate binding energetics, quantities that strongly correlate with OER activity.[12] Modulating the electronic structure of Ir-oxide to improve the oxygen binding energetics can thus theoretically enhance its intrinsic activity and lower the electricity and precious metal loading requirements of PEM electrolyzers. Alloying is one promising method to tune catalyst intrinsic activity that has previously led to substantial progress in catalyst development and fundamental understanding of Pt-based catalysts for the oxygen reduction reaction (ORR).[13–20] Recent work has investigated similar strategies to enhance the performance of Ir-based materials as OER catalysts. For example, acid-stable, inert materials such as W, Sn, Nb, and Ti have been added in an effort to dilute and stabilize Ir catalysts;[21–23] however, such materials generally demonstrate similar performance to pure Ir-oxide. Unstable transition metals (TM) like Ni,[24–27] Co,[26,27] Fe,[28] Mn,[29] and Cu[30] have also been incorporated into Ir catalysts in an effort to modify the intrinsic OER activity. Indeed, Ir-Ni bimetallic oxides[25] and IrCo oxide nanowires[27] have recently shown enhanced specific activity compared to Ir oxide. Additionally, surface leached Ir-based crystalline materials such as $SrIrO_3$ have

led to substantial improvements in Ir intrinsic activity by stabilizing unique surface site geometries.[31] While well-defined systematic studies of surface-leached alloy systems have led to enhanced activity and fundamental insight for Pt-based ORR catalysts, few analogous studies of Ir-based materials for the OER have been performed.

This work systematically explores the OER activity and stability of electrochemically oxidized Ir alloys in acidic electrolyte to identify improved chemistries and provide insight into structure-function relationships. Electron beam evaporation was utilized to co-deposit compact thin films of Ir, $IrSn_2$, IrCr, IrTi, and IrNi. Alloy composition was found to impact material performance with the IrCr system demonstrating enhanced specific activity over Ir-oxide and the highest stability of the alloys tested. Density functional theory (DFT) modeling indicates that the electrochemical leaching observed experimentally may stabilize highly active Cr dopant sites with near optimal adsorbate energetics leading to enhanced OER activity over pure Ir-oxide. Through controlled material synthesis, advanced characterization, and theoretical modeling, this study elucidates material performance trends and highlights the potential for further nanostructuring of the IrCr materials system to improve PEM electrolyzer performance and reduce precious metal requirements.

RESULTS

Film Synthesis and Characterization. Electron beam co-evaporation was used to deposit thin films of Ir, $IrSn_2$, IrCr, IrTi, and IrNi onto fluorinated tin oxide (FTO) substrates (see Supporting Information for details). Cross-sectional scanning electron microscopy (SEM) (Figure 1a-b) illustrates that the films form dense, conformal 50-60 nm coatings. Grazing incidence X-ray diffraction (GI-XRD) analysis (Figure 1) indicates that electron beam co-evaporation results in catalyst films with no evidence of phase separation, which is commonly observed for other Ir-based catalyst materials.[21,32,33] The Ir, IrCr, and IrNi films are crystalline, matching the reference patterns of their stoichiometric metallic alloys. On the contrary, $IrSn_2$ shows poor crystallinity with no diffraction features, indicating that it is amorphous. The crystal structures corresponding to the matching reference patterns (Figure 1) illustrate that the different alloys impart unique geometric modifications with IrNi forming a strained solid solution of the metallic Ir face-centered cubic structure with

3.5% lattice compression and IrCr forming a hexagonal unit cell. Enhanced (111), (200), and (111) reflections observed for Ir, IrCr, and IrNi, respectively, suggest that crystalline films are preferentially oriented. IrTi displays one broad diffraction peak, consistent with either preferentially oriented IrTi or strained metallic Ir; further differentiation between these possibilities is challenging as there are no additional XRD peaks.

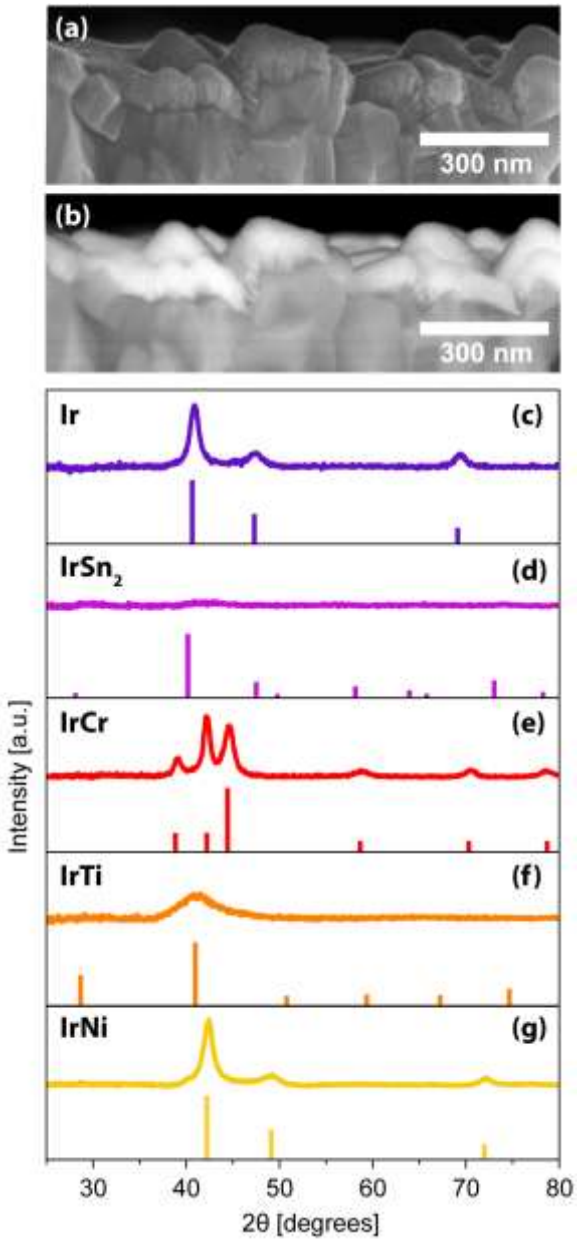

Figure 1. (a) Secondary electron (SE) and (b) back-scattered electron (BSE) SEM micrographs of a typical Ir alloy film on an FTO substrate (shown: $IrCr_{ox}$ after quasi-steady state OER electrochemical testing). The Ir-based film is most evident as the bright top layer visible in BSE mode. GI-XRD of Ir (c), $IrSn_2$ (d), IrCr (e), IrTi (f), and IrNi (g)

deposited on amorphous glass substrates. Experimental patterns are shown as the top curve while reference patterns are shown on the bottom of each graph. Reference patterns for the stoichiometric alloys: Ir (00-006-0598), $IrSn_2$ (01-073-2713), IrCr (04-001-1114), IrTi (01-074-5949), and IrNi (04-001-3158).

Electrochemical Performance. The electrocatalytic activity of the Ir-alloy films for the OER was evaluated in 0.5 M sulfuric acid with quasi steady state polarization (30 s potential holds at each electrode potential step, see Supporting Information for details). To emphasize that materials are electrochemically oxidized during testing, bimetallic systems are referred to as IrM_{ox} after electrochemical testing. Figure 2 and Table S2 show the geometric activity (electrode area-based) of the catalyst films while Figure S10 shows the cyclic voltammograms. Ir_{ox} was found to have comparable OER activity to other Ir films deposited by physical vapor deposition.[34] The geometric activity is highly affected by the material composition, with $IrCr_{ox}$ showing enhanced activity, $IrNi_{ox}$ showing commensurate activity, and $IrSn_{2,ox}$ and $IrTi_{ox}$ showing decreased OER geometric activity compared to Ir_{ox}. Table S2 summarizes the activity and Tafel slopes of the materials. $IrCr_{ox}$ was found to outperform Ir_{ox} with over 2.2 times the geometric current density at 1.65 V vs. RHE and a more desirable Tafel slope (59 versus 64 mV dec^{-1} for $IrCr_{ox}$ and Ir_{ox}, respectively). Additionally, while the Tafel slopes of all the other tested materials shift to 120-150 mV dec^{-1} at high current densities, often ascribed to a change in the reaction mechanism[35,36], $IrCr_{ox}$ maintains a low Tafel slope (83 mV dec^{-1}). This suggests that the transition in the rate determining step observed for the other materials is possibly delayed or prevented in $IrCr_{ox}$ as a result of modifications to the surface structure, electronic properties, or reaction mechanism.

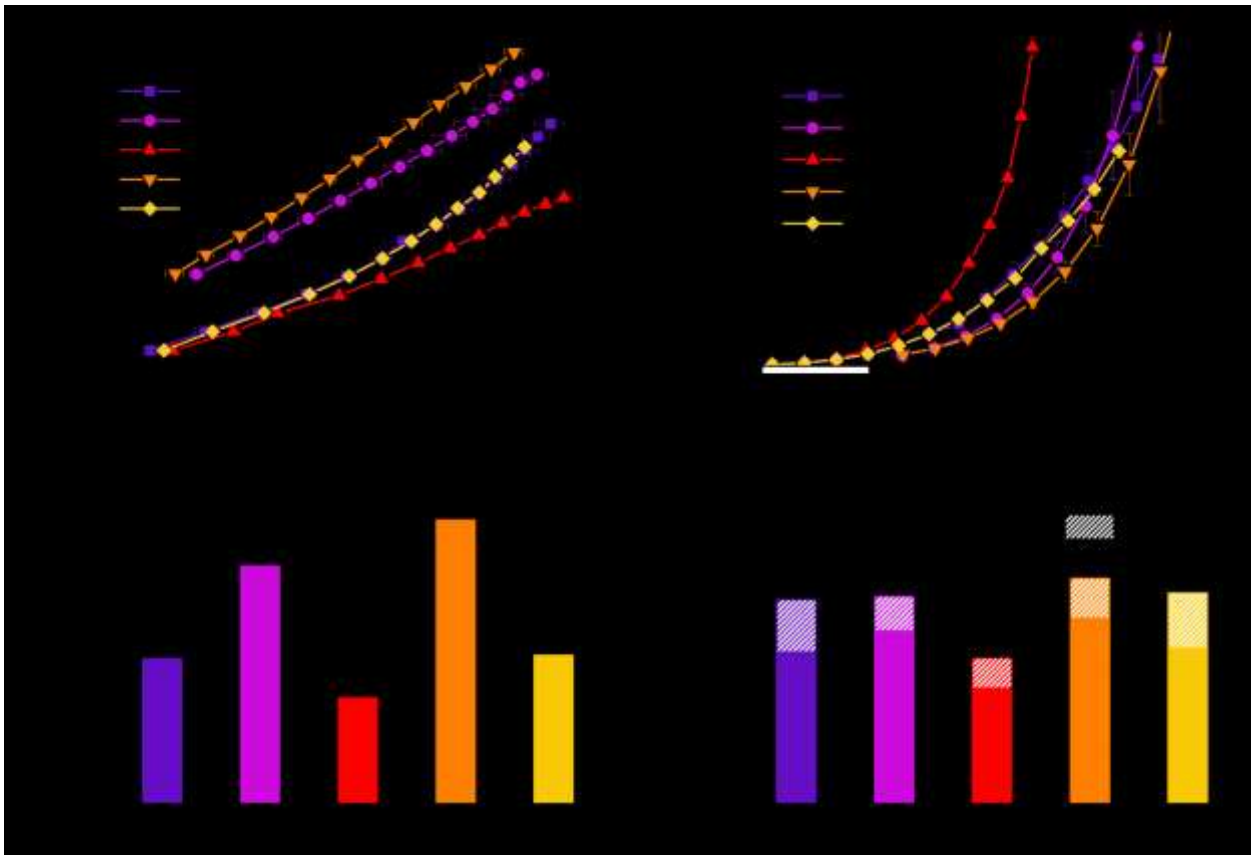

Figure 2. Electrochemical OER activity of electrochemically oxidized Ir, $IrSn_2$, IrCr, IrTi, and IrNi in 0.5 M H_2SO_4. (a) Geometric current density Tafel plot. (b) DLC-normalized specific activity. Overpotential required to achieve (c) 10 mA cm^{-2}_{geo} and (d) 10 A F^{-1} and 20 A F^{-1}.

To determine trends in intrinsic activity, OER measurements must be normalized to the electrochemically active surface area (ECSA). Unfortunately, there exists no ECSA measurement technique for Ir-based materials that is without considerable limitations. Redox peak integration, CO stripping, and hydrogen and mercury underpotential deposition either lead to significant errors, are inappropriate for Ir-oxides, or involve hazardous materials.[37] As the most appropriate method given current knowledge and limitations for the material systems studied here, non-faradaic capacitance was used to estimate the catalyst ECSA from the double layer capacitance.[7] To avoid errors and enable more straightforward comparisons to literature, a general specific capacitance was not assumed, and thus values are reported in A F^{-1} instead of A $cm^{-2}_{catalyst}$. For simplicity,

the double layer capacitance (DLC) per geometric surface area is henceforth referred to as the catalyst DLC.

Capacitive measurements and DLCs after OER polarization are shown in Figure S3 and Table S2, respectively, while DLC-normalized specific activities are shown in Figure 2. Upon surface area normalization, the specific activities of the catalyst materials show the same general trend as geometric activity ($IrTi_{ox}$ < $IrSn_{2,ox}$ < Ir_{ox} ~$IrNi_{ox}$ < $IrCr_{ox}$). Along with similar activities and Tafel slopes, Ir_{ox} and $IrNi_{ox}$ have comparable DLCs and thus exhibit nearly identical specific activities. In contrast to previously explored Ir-Ni mixed oxides,[25,38] the absence of enhanced activity for $IrNi_{ox}$ in this study may be due to differences in the synthesis route and thus the resulting structure. Although $IrTi_{ox}$ and $IrSn_{2,ox}$ show significantly reduced geometric activity compared to Ir_{ox}, their DLCs are a factor of four lower and thus their intrinsic activities are commensurate with that of Ir_{ox}. At higher current densities, $IrTi_{ox}$ and $IrSn_{2,ox}$ demonstrate commensurate if not enhanced activity over Ir_{ox} and $IrNi_{ox}$ due to their lower Tafel slopes. It is interesting to note that Sn and Ti, which typically form insulating oxides under OER potentials, do not appear to have a significant impact on the OER activity of $IrSn_{2,ox}$ and $IrTi_{ox}$, respectively (i.e. $IrSn_{2,ox}$ and $IrTi_{ox}$ have similar intrinsic activity to Ir_{ox}). Film conductivity, however, does not appear to directly correlate to activity as Ir_{ox} is expected to be the most conductive film, but it is not the most active of the materials tested. $IrCr_{ox}$ was found to have an DLC approximately 15% greater than Ir_{ox} and significantly greater specific activity with a >50 mV reduction in overpotential to achieve 20 A F^{-1} and two times the specific current density at 1.65 V vs. RHE compared to Ir_{ox}. In other words, after normalizing by the 15% greater capacitance (which is proportional to electrochemically accessible surface area), $IrCr_{ox}$ still has a two times greater specific activity than Ir_{ox}. This improvement in specific activity suggests that Cr is playing an important role to enhance the OER catalytic activity.

Pre and Post-Electrochemistry Characterization. Prior to electrochemical testing, X-ray photoelectron spectroscopy (XPS) shows that the as-synthesized films have near stoichiometric surface compositions with slight surface enrichment of the non-precious metal for $IrSn_2$, IrTi, and IrCr (Figure 3b). Through shifts in the Ir 4f peaks, XPS analysis illustrates that alloying alters the Ir electronic environment (see Figure 3a, Figure S2, and

Table S1). While the Ir catalyst film has an Ir $4f_{7/2}$ peak (61.8 eV) consistent with an IrO_2-like surface oxide,[39] the Ir $4f_{7/2}$ peaks of the majority of the alloyed materials are shifted to substantially lower energies; IrCr, $IrSn_2$, IrNi, and IrTi have Ir $4f_{7/2}$ peaks at 61.2, 60.5, 60.5, and 60.1 eV, respectively. These values are near or even slightly below that of metallic Ir^0 at 60.8 eV.[40] While binding energy shifts to values below the metallic reference are not commonly reported for Ir materials, similar 4f XPS shifts have been observed for Pt in Pt-Cu alloys.[41] XPS spectra for Sn, Cr, Ti, and Ni from the Ir-based alloys (Figure S2) show that these elements have varying degrees of oxidation with the spectra for most elements shifted to higher binding energies than those expected for the pure metallic materials (Table S1).

To provide insight into material evolution after electrochemistry and identify structure-function relationships, materials characterization post OER quasi steady-state polarization was performed. GI-XRD illustrates that the synthesized materials maintain their original bulk crystallinity (Figure S4), while XPS evidences changes in the catalyst surface. All materials undergo Ir surface-enrichment following OER testing (Figure 3b) with $IrSn_{2,ox}$, $IrTi_{ox}$, $IrCr_{ox}$ and $IrNi_{ox}$ having non-noble metal surface concentrations of 55, 40, 20, and 12 at%, respectively. Angle resolved XPS indicates that these compositions are constant for incident angles from 10 to 90° (see Figure S11), however, film roughness may decrease the reliability of these measurements. The relatively high concentration of the non-noble metal component in $IrTi_{ox}$ and $IrSn_{2,ox}$ at the catalyst surface observed by XPS may result in decreased conductivity or specific capacitance compared to electrochemically oxidized Ir resulting in the low DLCs observed for these alloys.[23] In contrast, the relatively low near-surface Ni content in $IrNi_{ox}$ compared to the non-noble metal surface content of the other films and its similar bulk crystal structure to Ir may explain the near-identical geometric and specific activity of $IrNi_{ox}$ and Ir_{ox}. For $IrCr_{ox}$, the notable Cr surface concentration after electrochemical testing indicates that Cr could play an influential role in catalysis by altering the Ir electronic structure, crystal structure, or the OER active site (see theoretical results and discussion below).

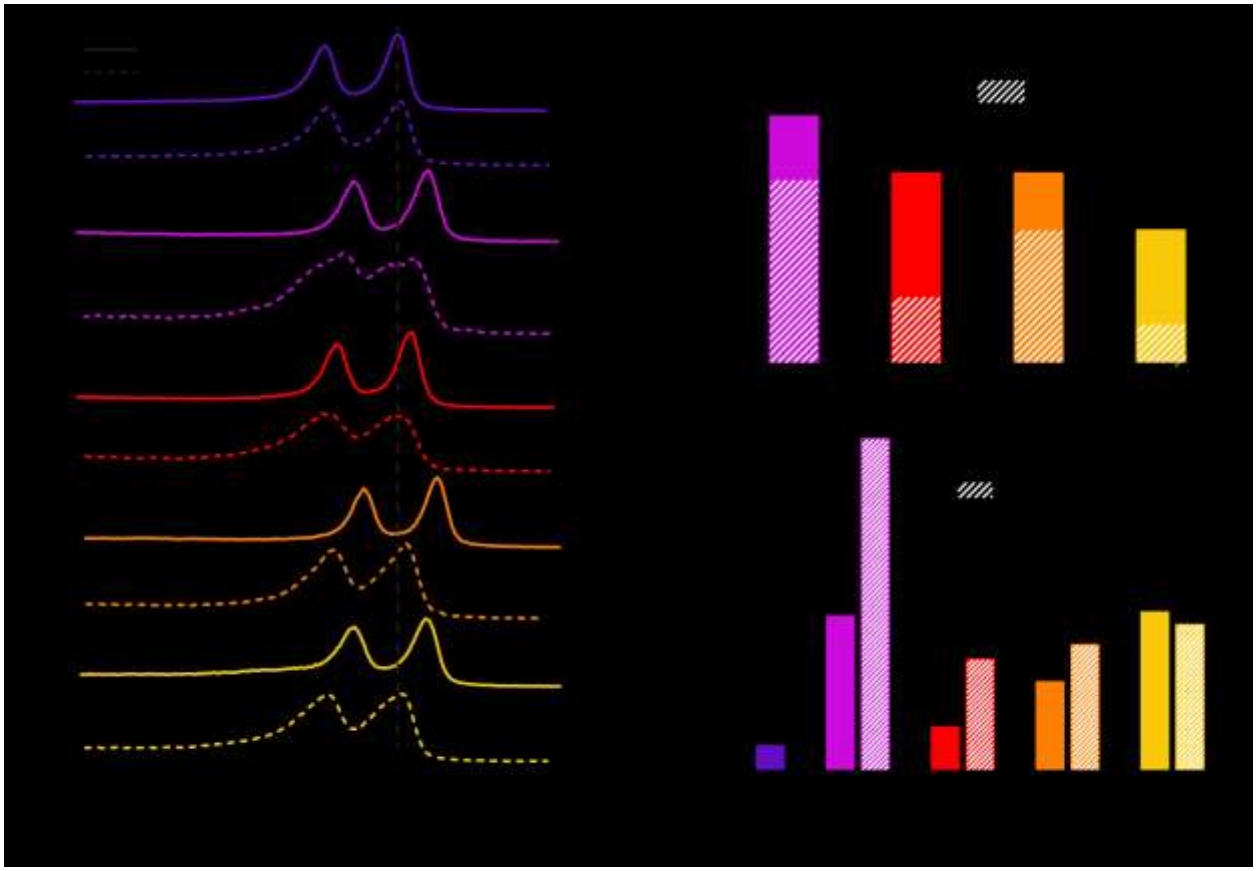

Figure 3. (a) XPS of Ir 4f peaks before (solid lines) and after OER testing (dashed lines). The black vertical line is provided to guide the eye. (b) XPS determined surface composition represented as non-noble alloy metal, M (i.e. Sn, Cr, Ti, or Ni), atomic concentration before (solid bars) and after quasi steady-state OER polarization (striped bars). All non-noble metals decrease in concentration but are still present in the near surface region after testing. (c) ICP-MS measured Ir (solid bars) and non-noble metal (striped bars) dissolution percentage of total loaded amount (determined from quartz crystal microbalance (QCM) measurements during deposition) of each metal after 6 h chronopotentiometric stability testing at 10 mA cm^{-2}_{geo} in 0.5 M H_2SO_4. Over 100% Sn loss is reflective of small errors in composition estimation from QCM measurements and electrolyte evaporation during stability testing.

In addition to changes in surface composition, the electronic structures of the Ir films are significantly altered after electrochemical quasi steady-state testing (Figure 3a, Figure S2, and Table S3). XPS analysis indicates that the Ir 4f peaks of all the alloys shift to higher binding energies after OER polarization due to the applied oxidative potentials. While the Ir 4f peaks of most materials resemble an IrO_2-like oxide, the peaks of $IrSn_{2,ox}$ and $IrTi_{ox}$ remain at lower binding energies than would be expected for a typical rutile-IrO_2 or amorphous IrO_x.[40] These shifts are consistent with electronic modifications of the Ir due

to the higher non-noble metal surface content observed for these materials. XPS analysis of the non-noble metal components (Figure S2) reveals that they are in predominately oxidized states following OER testing with the Cr in $IrCr_{ox}$ resembling a CrO_2 or Cr_2O_3-type oxide (see Supporting Information for details).[42,43]

To further probe material changes during the OER, inductively coupled plasma mass spectroscopy (ICP-MS) was used to quantify catalyst dissolution into the electrolyte during electrochemical stability measurements. Specifically, the dissolution was quantified after 2 h and 6 h chronopotentiometric stability tests at 10 mA cm^{-2}_{geo} as the percentage dissolved relative to the starting amount in each catalyst film (Figure 3c and Figure S6). The chronopotentiometry (Figure S5) illustrates activity degradation for all catalyst films, with $IrCr_{ox}$ and $IrTi_{ox}$ showing the smallest increase in overpotential over the 6 h stability test (9 and 5 mV h^{-1}, respectively, compared to 22 mV h^{-1} for Ir_{ox}). Non-noble metal dissolution increases as Cr < Ti < Ni < Sn and occurs more rapidly during the first two hours of testing (Figure S6). For $IrCr_{ox}$ and $IrTi_{ox}$, non-noble metal dissolution after the first two hours of stability testing proceeds at a rate equivalent to the Ir dissolution rate, consistent with the formation and maintenance of an Ir-rich surface layer as was observed in XPS. Complete Sn dissolution observed via ICP-MS is consistent with the complete loss in activity of $IrSn_2$ during 6 h stability testing. For all materials, Ir dissolution is generally lower than that of the corresponding non-noble metal consistent with Ir surface enrichment observed in XPS, and increases in the order of Ir_{ox} < $IrCr_{ox}$ < $IrTi_{ox}$ < $IrNi_{ox}$ ~ $IrSn_{2,ox}$. The bimetallic materials potentially experience enhanced Ir dissolution compared to the pure Ir_{ox} film as a result of the formation of less stable Ir sites during non-noble metal leaching. Due to the initial metallic nature of these materials, all Ir dissolution rates observed here are greater than those expected for pre-oxidized Ir materials.[44,45] Of the alloys tested, $IrCr_{ox}$ demonstrates the highest activity and stability to dissolution under OER conditions with further improvements in stability possible through oxidative pretreatments.[44–46]

Theoretical Activity of $IrCr_{ox}$. The origin of OER activity enhancement in $IrCr_{ox}$ over Ir_{ox} was investigated using density functional theory (DFT) calculations. Consistent with the post-electrochemistry XPS and as the most stable Ir oxide phase,[47] rutile IrO_2 was used

as the catalyst model structure. Given the low surface concentration of Cr after OER testing (20 at%), $IrCr_{ox}$ was modeled as Cr-doped IrO_2 with Cr atoms replacing Ir at different positions in the rutile-IrO_2 crystal. This type of Cr-doped structure is consistent with our post-electrochemistry XPS analysis which shows that Cr resembles a CrO_2-type oxide (see Figure 3, Figure S2 and Table S3 for XPS analysis). By simulating pristine surfaces, we neglect any surface reconstruction effects, which along with maintaining a uniform crystal structure between the IrO_2 and $IrCr_{ox}$ systems allows us to isolate the effect of doping from other structural effects, as well as reducing the computational expense considerably. The Cr-doped IrO_2 structure studied herein is similar to surface-doped structures employed to model other rutile systems.[48–51] Both the (110) and (100) surfaces of these materials were modeled due to their high activity and stability for the OER. [31,52,53]

Catalyst activity was assessed by computing the thermodynamic overpotential, η_{theory}, the overpotential beyond which all reaction steps are thermodynamically favorable. Specifically, the theoretical overpotential for the commonly utilized associative OER mechanism[12,54–58] (using *OH, *O, and *OOH as the OER intermediates) can be computed by evaluating the following equation:

$$\eta_{theory}=\max[\Delta G_{*OH}, \Delta G_{*O}-\Delta G_{*OH}, \Delta G_{*OOH}-\Delta G_{*O}, 4.92eV-\Delta G_{*OOH}]-1.23\ V \quad (1)$$

Using this methodology, the activity was computed for several Ir and Cr-substituted sites in the IrO_2 structure (see Table S5 for full list of modeled sites and energies. For further details on calculating the adsorption free energies see the Computational Details in the Supporting Information.).

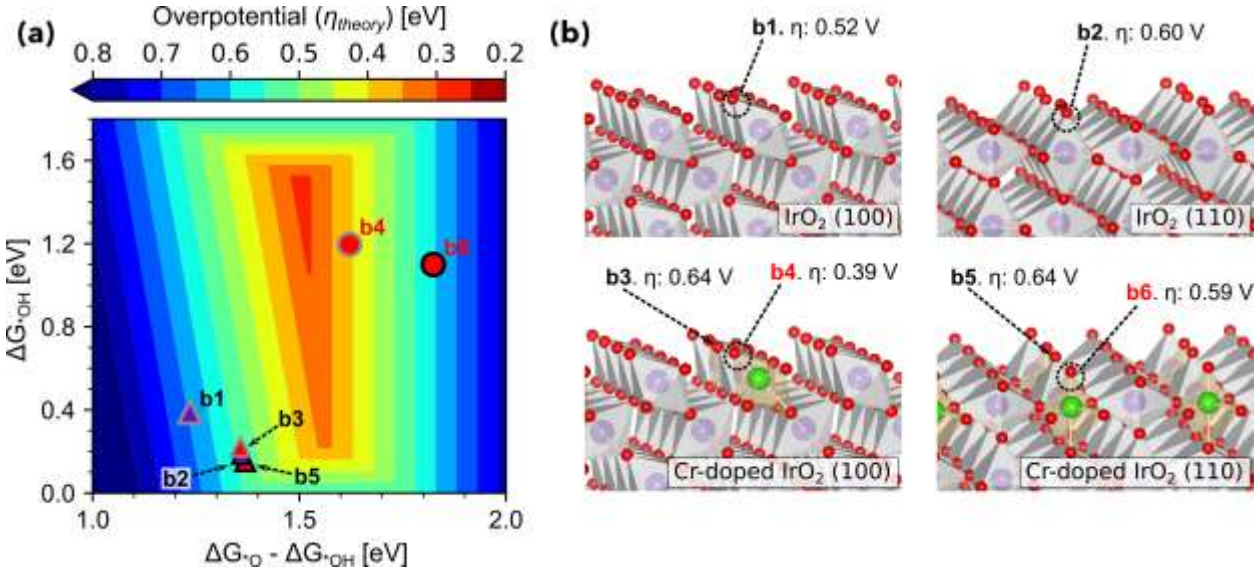

Figure 4. (a) OER activity volcano plot constructed with ΔG_{*O}-ΔG_{*OH} and ΔG_{*OH} descriptors and with the*OOH vs. *OH scaling fit shown in Figure S8. Sites from pure rutile-IrO_2 are depicted in purple while sites from Cr-doped IrO_2 are in red. Circles and triangles correspond to Cr- and Ir-active sites, respectively. Theoretical overpotentials corresponding to surfaces cut along the (110) plane are represented by black borders, while grey borders correspond to the (100) facet. Additional calculated sites are provided in Figure S7. (b) Corresponding structures and overpotentials of active sites from (a). Atom color: Ir (purple), Cr (green), and O (red). The structures and corresponding energies are also available at Catalysis-Hub.org.[59,60].

The predicted theoretical overpotentials for various sites in IrO_2 and Cr-doped IrO_2 are compared on an OER activity volcano plot using G_{*O}-ΔG_{*OH} and ΔG_{*OH} descriptor energies in Figure 4a. A linear scaling relation between *OOH and *OH intermediates was used to account for the *OOH dependence of η_{theory} (see Figure S8). The theoretical overpotentials of the pure rutile-IrO_2 (100) and (110) surface sites are 0.52 V and 0.6 V, respectively, and lie on the strong binding side of the OER activity volcano (see Figure 4b for corresponding structures). These overpotentials differ from the results of Seitz and co-workers[31] due to our more physical inclusion of spin-polarization, which changes the adsorption energies by ~0.2 eV (see Supporting Information for further discussion).

OER intermediates bind slightly stronger on the (110) facet than on the (100) facet due to the lower average oxidation state of the active surface metal atoms on the (110) facet (see Bader charge analysis in Table S6). Upon doping the surfaces with Cr, the activity

and oxygen adsorbate binding energies of Ir sites stay relatively unchanged (< 0.15 eV change), indicating strong metallic screening at the surface. Interestingly, the Cr sites in Cr-doped IrO_2 have significantly weakened binding of the OER intermediates relative to Ir sites (+1.3 eV for *O and +0.9 eV for OH* compared to Ir sites). More importantly, ΔG_{*O} is weakened more than ΔG_{*OH} (see Figure S8) which results in the effective increase of the ΔG_{*O}-ΔG_{*OH} energy (shown in Figure 4a). This combined effect lowers the predicted theoretical overpotentials on the Cr-dopant sites compared to the Ir sites in pure IrO_2 with the overpotential decreasing from 0.52 V to 0.39 V on the (100) surface and from 0.60 V to 0.59 V on the (110) surface (see Figure 4b for corresponding structures). The calculated Bader charge of the Cr dopant in bulk rutile-IrO_2 (+1.72 e^-) is nearly identical to the charge of the Cr^{+4} cation in bulk rutile CrO_2 (+1.77 e^-) and therefore effectively resembles a Cr^{+4} site in the conductive environment of IrO_2 (see Table S6 for full Bader charge analysis). Additional calculations on Ir sites with sub-surface Cr dopants (Figure S7) yielded similar theoretical overpotentials to those calculated for the other Ir-sites. These results suggest that surface Cr atoms are predominately responsible for the experimentally observed enhanced specific activity of $IrCr_{ox}$ compared to Ir_{ox}. The identification of highly active Cr sites is consistent with the enhanced OER activity observed for other Cr-based systems[48,50,51,61,62] and motivates optimization and nanostructuring of the $IrCr_{ox}$ system.

CONCLUSION

In conclusion, Ir alloys of $IrSn_2$, IrCr, IrTi, and IrNi were synthesized via dual electron beam evaporation and evaluated for OER catalysis in acid. OER activities were found to be highly dependent on catalyst film composition with geometric and specific activity increasing as follows: $IrTi_{ox}$ < $IrSn_{2,ox}$ < Ir_{ox} ~ $IrNi_{ox}$ < $IrCr_{ox}$. The $IrCr_{ox}$ catalyst outperforms pure Ir_{ox} with over two times greater activity based on both the geometric and specific current density at 1.65 V vs. RHE. Post-electrochemical characterization of the catalyst films illustrates that metal leaching results in an Ir-enriched surface that still contains a significant amount of non-noble metal species. Of the mixed metal oxides, the $IrCr_{ox}$ catalyst also showed the highest electrochemical and material stability. To identify the origin of the enhanced catalytic performance of $IrCr_{ox}$, DFT was utilized to calculate the

theoretical OER activity of Cr-doped IrO_2 and pure IrO_2. Cr^{+4}-dopant sites were found to have weaker and more optimal oxygen binding energies compared to Ir-sites in both the pure and doped IrO_2, potentially accounting for the observed enhanced activity of $IrCr_{ox}$ compared to Ir_{ox}. The identification of such highly active dopant sites with near optimal oxygen binding energies in the Cr-doped IrO_2 structure illustrates the potential of the $IrCr_{ox}$ system for further optimization and nanostructuring as well as motivates a search for other materials as potential hosts for active Cr^{+4} sites. The synthesis of high surface area $IrCr_{ox}$ is an important future direction to improve geometric-based OER activity. Through systematic studies of controlled materials, promising OER catalysts such as $IrCr_{ox}$ can be identified, optimized, and analyzed computationally to elucidate structure-function relationships and motivate chemistries toward improved water electrolysis.

ASSOCIATED CONTENT

Supporting Information

Experimental methods, computational methods, and additional material and electrochemical characterization are available in the Supporting Information.

ACKNOWLEDGEMENTS

This work was supported by the U.S. Department of Energy, Chemical Sciences, Geosciences, and Biosciences (CSGB) Division of the Office of Basic Energy Sciences, via Grant DE-AC02-76SF00515 to the SUNCAT Center for Interface Science and Catalysis. A.S. acknowledges fellowship support from the National Science Foundation Graduate Research Fellowship Program (NSF-GRFP). Any opinions, findings, and conclusions or recommendations expressed in this material are those of the authors and do not necessarily reflect the views of the National Science Foundation. Part of this work was performed at the Stanford Nano Shared Facilities (SNSF), supported by the National Science Foundation under award ECCS-1542152. The authors would like to acknowledge the use of the computer time allocation for the Transition metal-oxide and metal surfaces: applications and reactivity trends in catalysis at the National Energy Research Scientific Computing Center, a DOE Office of Science User Facility supported

by the Office of Science of the U.S. Department of Energy under Contract No. DE-AC02-05CH11231.

REFERENCES

(1) Katsounaros, I.; Cherevko, S.; Zeradjanin, A. R.; Mayrhofer, K. J. J. Oxygen Electrochemistry as a Cornerstone for Sustainable Energy Conversion. *Angew. Chemie Int. Ed.* **2014**, *53* (1), 102–121.

(2) Fabbri, E.; Habereder, A.; Waltar, K.; Kötz, R.; Schmidt, T. J. Developments and Perspectives of Oxide-Based Catalysts for the Oxygen Evolution Reaction. *Catal. Sci. Technol.* **2014**, *4* (11), 3800–3821.

(3) Reier, T.; Nong, H. N.; Teschner, D.; Schlögl, R.; Strasser, P. Electrocatalytic Oxygen Evolution Reaction in Acidic Environments - Reaction Mechanisms and Catalysts. *Adv. Energy Mater.* **2017**, *7* (1), 1601275.

(4) Simbolotti, G. Hydrogen Production & Distribution. *IEA Energy Technol. Essentials* **2007**, No. 1, 3–6.

(5) Rostrup-Nielsen, J. R.; Sehested, J.; Noerskov, J. K. Hydrogen and Synthesis Gas by Steam- and CO2 Reforming. *ChemInform* **2003**, *34* (17), 65–139.

(6) Annual Merit Review; U.S. Department of Energy. *H2 at Scale: Deeply Decarbonizing Our Energy System*; Washington, D.C., 2016.

(7) McCrory, C. C. L.; Jung, S.; Ferrer, I. M.; Chatman, S. M.; Peters, J. C.; Jaramillo, T. F. Benchmarking Hydrogen Evolving Reaction and Oxygen Evolving Reaction Electrocatalysts for Solar Water Splitting Devices. *J. Am. Chem. Soc.* **2015**, *137* (13), 4347–4357.

(8) Jamesh, M.-I.; Sun, X. Recent Progress on Earth Abundant Electrocatalysts for Oxygen Evolution Reaction (OER) in Alkaline Medium to Achieve Efficient Water Splitting – A Review. *J. Power Sources* **2018**, *400* (July), 31–68.

(9) Carmo, M.; Fritz, D. L.; Mergel, J.; Stolten, D. A Comprehensive Review on PEM

Water Electrolysis. *Int. J. Hydrogen Energy* **2013**, *38* (12), 4901–4934.

(10) Levene, J. I.; Mann, M. K.; Margolis, R. M.; Milbrandt, A. An Analysis of Hydrogen Production from Renewable Electricity Sources. *Sol. Energy* **2007**, *81* (6), 773–780.

(11) Ayers, K. E.; Capuano, C.; Anderson, E. B. Recent Advances in Cell Cost and Efficiency for PEM-Based Water Electrolysis. *ECS Trans.* **2012**, *41* (10), 15–22.

(12) Man, I. C.; Su, H. Y.; Calle-Vallejo, F.; Hansen, H. a.; Martínez, J. I.; Inoglu, N. G.; Kitchin, J.; Jaramillo, T. F.; Nørskov, J. K.; Rossmeisl, J. Universality in Oxygen Evolution Electrocatalysis on Oxide Surfaces. *ChemCatChem* **2011**, *3* (7), 1159–1165.

(13) Escudero-Escribano, M.; Jensen, K. D.; Jensen, A. W. Recent Advances in Bimetallic Electrocatalysts for Oxygen Reduction: Design Principles, Structure-Function Relations and Active Phase Elucidation. *Curr. Opin. Electrochem.* **2018**, *8*, 135–146.

(14) Hernandez-Fernandez, P.; Masini, F.; McCarthy, D. N.; Strebel, C. E.; Friebel, D.; Deiana, D.; Malacrida, P.; Nierhoff, A.; Bodin, A.; Wise, A. M.; Nielsen, J. H.; Hansen, T. W.; Nilsson, A.; Stephens, I. E. L.; Chorkendorff, I. Mass-Selected Nanoparticles of PtxY as Model Catalysts for Oxygen Electroreduction. *Nat. Chem.* **2014**, *6* (8), 732–738.

(15) Choi, S.-I.; Xie, S.; Shao, M.; Odell, J. H.; Lu, N.; Peng, H.; Protsailo, L.; Guerrero, S.; Park, J.; Xia, X.; Wang, J.; Kim, M. J.; Xia, Y. Synthesis and Characterization of 9 Nm Pt–Ni Octahedra with a Record High Activity of 3.3 A/Mg Pt for the Oxygen Reduction Reaction. *Nano Lett.* **2013**, *13* (7), 3420–3425.

(16) Greeley, J.; Stephens, I. E. L.; Bondarenko, a S.; Johansson, T. P.; Hansen, H. a; Jaramillo, T. F.; Rossmeisl, J.; Chorkendorff, I.; Nørskov, J. K. Alloys of Platinum and Early Transition Metals as Oxygen Reduction Electrocatalysts. *Nat. Chem.* **2009**, *1* (7), 552–556.

(17) Stephens, I. E. L.; Bondarenko, A. S.; Grønbjerg, U.; Rossmeisl, J.; Chorkendorff,

I. Understanding the Electrocatalysis of Oxygen Reduction on Platinum and Its Alloys. *Energy Environ. Sci.* **2012**, *5* (5), 6744.

(18) Escudero-Escribano, M.; Malacrida, P.; Hansen, M. H.; Vej-Hansen, U. G.; Velazquez-Palenzuela, A.; Tripkovic, V.; Schiotz, J.; Rossmeisl, J.; Stephens, I. E. L.; Chorkendorff, I. Tuning the Activity of Pt Alloy Electrocatalysts by Means of the Lanthanide Contraction. *Science (80-.).* **2016**, *352* (6281), 73–76.

(19) Huang, X.; Zhao, Z.; Cao, L.; Chen, Y.; Zhu, E.; Lin, Z.; Li, M.; Yan, A.; Zettl, A.; Wang, Y. M.; Duan, X.; Mueller, T.; Huang, Y. High-Performance Transition Metal – Doped Pt3Ni Octahedra for Oxygen Reduction Reaction. *Science (80-.).* **2015**, *348* (2009), 1230–1234.

(20) Kitchin, J. R.; Nørskov, J. K.; Barteau, M. A.; Chen, J. G. Role of Strain and Ligand Effects in the Modification of the Electronic and Chemical Properties of Bimetallic Surfaces. *Phys. Rev. Lett.* **2004**, *93* (15), 4–7.

(21) Kumari, S.; Ajayi, B. P.; Kumar, B.; Jasinski, J. B.; Sunkara, M. K.; Spurgeon, J. M. A Low-Noble-Metal W1−xIrxO3−δ Water Oxidation Electrocatalyst for Acidic Media via Rapid Plasma Synthesis. *Energy Environ. Sci.* **2017**, *10* (11), 2432–2440.

(22) Kadakia, K.; Datta, M. K.; Velikokhatnyi, O. I.; Jampani, P. H.; Kumta, P. N. Fluorine Doped (Ir,Sn,Nb)O2 Anode Electro-Catalyst for Oxygen Evolution via PEM Based Water Electrolysis. *Int. J. Hydrogen Energy* **2014**, *39* (2), 664–674.

(23) Kokoh, K. B.; Mayousse, E.; Napporn, T. W.; Servat, K.; Guillet, N.; Soyez, E.; Grosjean, A.; Rakotondrainibé, A.; Paul-Joseph, J. Efficient Multi-Metallic Anode Catalysts in a PEM Water Electrolyzer. *Int. J. Hydrogen Energy* **2014**, *39* (5), 1924–1931.

(24) Nong, H. N.; Oh, H. S.; Reier, T.; Willinger, E.; Willinger, M. G.; Petkov, V.; Teschner, D.; Strasser, P. Oxide-Supported IrNiOx Core-Shell Particles as Efficient, Cost-Effective, and Stable Catalysts for Electrochemical Water Splitting SI. *Angew. Chemie - Int. Ed.* **2015**, *54* (10), 2975–2979.

(25) Reier, T.; Pawolek, Z.; Cherevko, S.; Bruns, M.; Jones, T.; Teschner, D.; Selve, S.; Bergmann, A.; Nong, H. N.; Schlögl, R.; Mayrhofer, K. J. J.; Strasser, P. Molecular Insight in Structure and Activity of Highly Efficient, Low-Ir Ir-Ni Oxide Catalysts for Electrochemical Water Splitting (OER). *J. Am. Chem. Soc.* **2015**, *137* (40), 13031–13040.

(26) Pi, Y.; Shao, Q.; Wang, P.; Guo, J.; Huang, X. General Formation of Monodisperse IrM (M = Ni, Co, Fe) Bimetallic Nanoclusters as Bifunctional Electrocatalysts for Acidic Overall Water Splitting. *Adv. Funct. Mater.* **2017**, *27* (27), 1–8.

(27) Alia, S. M.; Shulda, S.; Ngo, C.; Pylypenko, S.; Pivovar, B. S. Iridium-Based Nanowires as Highly Active, Oxygen Evolution Reaction Electrocatalysts. *ACS Catal.* **2018**, No. 37, 2111–2120.

(28) Fu, L.; Cheng, G.; Luo, W. Colloidal Synthesis of Monodisperse Trimetallic IrNiFe Nanoparticles as Highly Active Bifunctional Electrocatalysts for Acidic Overall Water Splitting. *J. Mater. Chem. A* **2017**, *5* (47), 24836–24841.

(29) Ghadge, S. D.; Patel, P. P.; Datta, M. K.; Velikokhatnyi, O. I.; Kuruba, R.; Shanthi, P. M.; Kumta, P. N. Fluorine Substituted (Mn,Ir)O2:F High Performance Solid Solution Oxygen Evolution Reaction Electro-Catalysts for PEM Water Electrolysis. *RSC Adv.* **2017**, *7* (28), 17311–17324.

(30) Wang, C.; Moghaddam, R. B.; Bergens, S. H. Active, Simple Iridium-Copper Hydrous Oxide Electrocatalysts for Water Oxidation. *J. Phys. Chem. C* **2017**, *121* (10), 5480–5486.

(31) Seitz, L. C.; Dickens, C. F.; Nishio, K.; Hikita, Y.; Montoya, J.; Doyle, A.; Kirk, C.; Vojvodic, A.; Hwang, H. Y.; Norskov, J. K.; Jaramillo, T. F. A Highly Active and Stable IrO x /SrIrO 3 Catalyst for the Oxygen Evolution Reaction. *Science (80-.).* **2016**, *353* (6303), 1011–1014.

(32) Chen, G.; Chen, X.; Yue, P. L. Electrochemical Behavior of Novel Ti/IrO x −Sb 2 O 5 −SnO 2 Anodes. *J. Phys. Chem. B* **2002**, *106* (17), 4364–4369.

(33) Oakton, E.; Lebedev, D.; Povia, M.; Abbott, D. F.; Fabbri, E.; Fedorov, A.; Nachtegaal, M.; Copéret, C.; Schmidt, T. J. IrO 2 -TiO 2 : A High-Surface-Area, Active, and Stable Electrocatalyst for the Oxygen Evolution Reaction. *ACS Catal.* **2017**, *7* (4), 2346–2352.

(34) Chen, Y. W.; Prange, J. D.; Dühnen, S.; Park, Y.; Gunji, M.; Chidsey, C. E. D.; McIntyre, P. C. Atomic Layer-Deposited Tunnel Oxide Stabilizes Silicon Photoanodes for Water Oxidation. *Nat. Mater.* **2011**, *10* (7), 539–544.

(35) Hu, J. Oxygen Evolution Reaction on IrO2-Based DSA® Type Electrodes: Kinetics Analysis of Tafel Lines and EIS. *Int. J. Hydrogen Energy* **2004**, *29* (8), 791–797.

(36) Diaz-Morales, O.; Raaijman, S.; Kortlever, R.; Kooyman, P. J.; Wezendonk, T.; Gascon, J.; Fu, W. T.; Koper, M. T. M. Iridium-Based Double Perovskites for Efficient Water Oxidation in Acid Media. *Nat. Commun.* **2016**, *7*, 12363.

(37) Alia, S. M.; Hurst, K. E.; Kocha, S. S.; Pivovar, B. S. Mercury Underpotential Deposition to Determine Iridium and Iridium Oxide Electrochemical Surface Areas. *J. Electrochem. Soc.* **2016**, *163* (11), F3051–F3056.

(38) Nong, H. N.; Gan, L.; Willinger, E.; Teschner, D.; Strasser, P. IrOx Core-Shell Nanocatalysts for Cost- and Energy-Efficient Electrochemical Water Splitting. *Chem. Sci.* **2014**, *5* (8), 2955–2963.

(39) Pfeifer, V.; Jones, T. E.; Velasco Vélez, J. J.; Massué, C.; Greiner, M. T.; Arrigo, R.; Teschner, D.; Girgsdies, F.; Scherzer, M.; Allan, J.; Hashagen, M.; Weinberg, G.; Piccinin, S.; Hävecker, M.; Knop-Gericke, A.; Schlögl, R. The Electronic Structure of Iridium Oxide Electrodes Active in Water Splitting. *Phys. Chem. Chem. Phys.* **2016**, *18* (4), 2292–2296.

(40) Pfeifer, V.; Jones, T. E.; Velasco Vélez, J. J.; Massué, C.; Arrigo, R.; Teschner, D.; Girgsdies, F.; Scherzer, M.; Greiner, M. T.; Allan, J.; Hashagen, M.; Weinberg, G.; Piccinin, S.; Hävecker, M.; Knop-Gericke, A.; Schlögl, R. The Electronic Structure of Iridium and Its Oxides. *Surf. Interface Anal.* **2016**, *48* (5), 261–273.

(41) Barrett, N. T.; Belkhou, R.; Thiele, J.; Guillot, C. A Core-Level Photoemission Spectroscopy Study of the Formation of Surface Alloy Cu Pt(111): Comparison with Pt Cu(111). *Surf. Sci.* **1995**, *331–333* (PART A), 776–781.

(42) Ikemoto, I.; Ishii, K.; Kinoshita, S.; Kuroda, H.; Alario Franco, M. A.; Thomas, J. M. X-Ray Photoelectron Spectroscopic Studies of CrO2 and Some Related Chromium Compounds. *J. Solid State Chem.* **1976**, *17* (4), 425–430.

(43) Allen, G. C.; Harris, S. J.; Jutson, J. A.; Dyke, J. M. A Study of a Number of Mixed Transition Metal Oxide Spinels Using X-Ray Photoelectron Spectroscopy. *Appl. Surf. Sci.* **1989**, *37* (1), 111–134.

(44) Jovanovič, P.; Hodnik, N.; Ruiz-Zepeda, F.; Arčon, I.; Jozinović, B.; Zorko, M.; Bele, M.; Šala, M.; Šelih, V. S.; Hočevar, S.; Gaberščček, M. Electrochemical Dissolution of Iridium and Iridium Oxide Particles in Acidic Media: Transmission Electron Microscopy, Electrochemical Flow Cell Coupled to Inductively Coupled Plasma Mass Spectrometry, and X-Ray Absorption Spectroscopy Study. *J. Am. Chem. Soc.* **2017**, *139* (36), 12837–12846.

(45) Cherevko, S.; Geiger, S.; Kasian, O.; Kulyk, N.; Grote, J.-P.; Savan, A.; Shrestha, B. R.; Merzlikin, S.; Breitbach, B.; Ludwig, A.; Mayrhofer, K. J. J. Oxygen and Hydrogen Evolution Reactions on Ru, RuO 2 , Ir, and IrO 2 Thin Film Electrodes in Acidic and Alkaline Electrolytes: A Comparative Study on Activity and Stability. *Catal. Today* **2016**, *262*, 170–180.

(46) Paoli, E. A.; Masini, F.; Frydendal, R.; Deiana, D.; Malacrida, P.; Hansen, T. W.; Chorkendorff, I.; Stephens, I. E. L. Fine-Tuning the Activity of Oxygen Evolution Catalysts: The Effect of Oxidation Pre-Treatment on Size-Selected Ru Nanoparticles. *Catal. Today* **2016**, *262*, 57–64.

(47) Ono, S.; Brodholt, J. P.; Price, G. D. Structural Phase Transitions in IrO_2 at High Pressures. *J. Phys. Condens. Matter* **2008**, *20* (4), 045202.

(48) García-Mota, M.; Vojvodic, A.; Metiu, H.; Man, I. C.; Su, H.-Y.; Rossmeisl, J.;

Nørskov, J. K. Tailoring the Activity for Oxygen Evolution Electrocatalysis on Rutile TiO2(110) by Transition-Metal Substitution. *ChemCatChem* **2011**, *3* (10), 1607–1611.

(49) García-Mota, M.; Vojvodic, A.; Abild-Pedersen, F.; Nørskov, J. K. Electronic Origin of the Surface Reactivity of Transition-Metal-Doped TiO $_2$ (110). *J. Phys. Chem. C* **2013**, *117* (1), 460–465.

(50) Karlsson, R. K. B.; Cornell, A.; Pettersson, L. G. M. The Electrocatalytic Properties of Doped TiO2. *Electrochim. Acta* **2015**, *180*, 514–527.

(51) Lin, Y.; Tian, Z.; Zhang, L.; Ma, J.; Jiang, Z.; Deibert, B. J.; Ge, R.; Chen, L. Chromium-Ruthenium Oxide Solid Solution Electrocatalyst for Highly Efficient Oxygen Evolution Reaction in Acidic Media. *Nat. Commun.* **2019**, *10* (1), 162.

(52) Stoerzinger, K. A.; Qiao, L.; Biegalski, M. D.; Shao-Horn, Y. Orientation-Dependent Oxygen Evolution Activities of Rutile IrO $_2$ and RuO $_2$. *J. Phys. Chem. Lett.* **2014**, *5* (10), 1636–1641.

(53) Lee, Y.; Suntivich, J.; May, K. J.; Perry, E. E.; Shao-Horn, Y. Synthesis and Activities of Rutile IrO $_2$ and RuO $_2$ Nanoparticles for Oxygen Evolution in Acid and Alkaline Solutions. *J. Phys. Chem. Lett.* **2012**, *3* (3), 399–404.

(54) Rossmeisl, J.; Qu, Z.-W.; Zhu, H.; Kroes, G.-J.; Nørskov, J. K. Electrolysis of Water on Oxide Surfaces. *J. Electroanal. Chem.* **2007**, *607* (1–2), 83–89.

(55) Nørskov, J. K.; Rossmeisl, J.; Logadottir, a.; Lindqvist, L.; Kitchin, J. R.; Bligaard, T.; Jónsson, H. Origin of the Overpotential for Oxygen Reduction at a Fuel-Cell Cathode. *J. Phys. Chem. B* **2004**, *108* (46), 17886–17892.

(56) Friebel, D.; Louie, M. W.; Bajdich, M.; Sanwald, K. E.; Cai, Y.; Wise, A. M.; Cheng, M.-J.; Sokaras, D.; Weng, T.-C.; Alonso-Mori, R.; Davis, R. C.; Bargar, J. R.; Nørskov, J. K.; Nilsson, A.; Bell, A. T. Identification of Highly Active Fe Sites in (Ni,Fe)OOH for Electrocatalytic Water Splitting. *J. Am. Chem. Soc.* **2015**, *137* (3), 1305–1313.

(57) Bajdich, M.; García-Mota, M.; Vojvodic, A.; Nørskov, J. K.; Bell, A. T. Theoretical Investigation of the Activity of Cobalt Oxides for the Electrochemical Oxidation of Water. *J. Am. Chem. Soc.* **2013**, *135* (36), 13521–13530.

(58) Lu, Z.; Chen, G.; Li, Y.; Wang, H.; Xie, J.; Liao, L.; Liu, C.; Liu, Y.; Wu, T.; Li, Y.; Luntz, A. C.; Bajdich, M.; Cui, Y. Identifying the Active Surfaces of Electrochemically Tuned LiCoO2 for Oxygen Evolution Reaction. *J. Am. Chem. Soc.* **2017**, *139* (17), 6270–6276.

(59) Computational Data https://www.catalysis-hub.org/publications/StricklerSystematic2019 (accessed Aug 22, 2019).

(60) Winther, K. T.; Hoffmann, M. J.; Boes, J. R.; Mamun, O.; Bajdich, M.; Bligaard, T. Catalysis-Hub.Org, an Open Electronic Structure Database for Surface Reactions. *Sci. Data* **2019**, *6* (1), 75.

(61) Shao, C.; Zhang, F.; Li, X.; Zhang, J.; Jiang, Y.; Cheng, H.; Zhu, K. Influence of Cr Doping on the Oxygen Evolution Potential of SnO2/Ti and Sb-SnO2/Ti Electrodes. *J. Electroanal. Chem.* **2019**, *832* (July 2018), 436–443.

(62) Zhao, Z.; Schlexer Lamoureux, P.; Kulkarni, A.; Bajdich, M. Trends in Oxygen Electrocatalysis of *3 d* - Layered (Oxy)(Hydro)Oxides. *ChemCatChem* **2019**, *11* (15), cctc.201900846.